Journal of the Indian Chemical Society 100 (2023) 100926

Contents lists available at ScienceDirect

Journal of the Indian Chemical Society

journal homepage: www.journals.elsevier.com/journal-of-the-indian-chemical-society

DFT, ADMET, molecular docking and molecular dynamics studies of pyridoxal

Nadezhda A. Garkusha [a], Oksana P. Anikeeva [a], Imren Bayıl [b], Tugba Taskin-Tok [b,c,**], Damir A. Safin [a,d,*]

[a] University of Tyumen, Volodarskogo Str. 6, 625003, Tyumen, Russian Federation
[b] University of Gaziantep, Department of Bioinformatics and Computational Biology, Institute of Health Sciences, 27310, Gaziantep, Turkey
[c] University of Gaziantep, Department of Chemistry, Faculty of Arts and Sciences, 27310, Gaziantep, Turkey
[d] Scientific and Educational and Innovation Center for Chemical and Pharmaceutical Technologies, Ural Federal University named after the First President of Russia B.N. Yeltsin, Ekaterinburg, 620002, Russian Federation

ARTICLE INFO

Keywords:
Pyridine
Computational study
Density functional theory
Molecular docking
Molecular dynamics simulation
COVID-19

ABSTRACT

We report in silico studies of pyridoxal, which is of interest both as a precursor for further functionalization due to the presence of the aldehyde functionality, as well as a bioactive compound. So far, the crystal structure of pyridoxal has not been reported and, thus, we have optimized its structure both under water solvation and in gas phase using the DFT calculations. Under water solvation conditions the optimized structure of pyridoxal is 7.62 kcal/mol more favorable in comparison to that in gas phase. The DFT calculations were also applied to verify optical and electronic properties of the optimized structure of pyridoxal in water. The HOMO and LUMO were revealed to subtract a set of descriptors of the so-called global chemical reactivity as well as to probe pyridoxal as a potential corrosion inhibitor for some important metals used in implants. The title compound exhibits the best electron charge transfer from the molecule to the surface of Ni and Co. Some biological properties of pyridoxal were evaluated using the respective on-line tools. Molecular docking was additionally applied to study interaction of pyridoxal with some SARS-CoV-2 proteins as well as one of the monkeypox proteins. It was established that the title compound is active against all the applied proteins with the most efficient interaction with nonstructural protein 15 (endoribonuclease) and Omicron Spike protein of SARS-CoV-2. Pyridoxal was found to be also active against the studied monkeypox protein. Interaction of pyridoxal with nonstructural protein 15 (endoribonuclease) was further studied using molecular dynamics simulation.

1. Introduction

One of the key components of modern strategies to design drugs is heterocycles. Nowadays, main active components containing heterocycles with nitrogen, oxygen and sulfur atoms comprise about 80% of all drugs [1,2]. The pyridine-based compounds are of particular interest since they can posses a rich structural variety and demonstrate activity against diseases. Incorporation of substituents in the heterocyclic core is a powerfull tool to vary their biological activity [3–6]. An additional interest in the pyridine-based derivatives as medicines is currently due to the formation of covalent bonds with amino acid residues of proteins. This allows to use them for covalent inhibition of bacterial and viral proteins. Particularly, the pyridine derivatives are known to be pronounced cysteine protease inhibitors [7,8].

These days, the antiviral activity of the pyridine-based derivatives is also due to the SARS-CoV-2 coronavirus pandemic, which was announced by the World Health Organization (WHO) in March 2020. Unfortunately, about 755 million infections and more than 6.83 million deaths were reveled to date (middle of February 2023) [9]. Furthermore, new strains complicate the situation with COVID-19. To be said, that the newest agents for COVID-19 therapy are also constructed from the pyridine rings [10].

We have also been continuously interested in the chemistry of nitrogen-containing six-membered rings [11–18] as well as in computational analyses of compounds with the biological activity [19–29]. In the present work, we have focused on 3-hydroxy-5-(hydroxy

* Corresponding author. University of Tyumen, Volodarskogo Str. 6, 625003, Tyumen, Russian Federation.
** Corresponding author. University of Gaziantep, Department of Chemistry, Faculty of Arts and Sciences, 27310, Gaziantep, Turkey.
E-mail addresses: ttaskin@gantep.edu.tr, taskin.tugba@gmail.com (T. Taskin-Tok), damir.a.safin@gmail.com (D.A. Safin).

https://doi.org/10.1016/j.jics.2023.100926
Received 17 July 2022; Received in revised form 26 November 2022; Accepted 28 January 2023
Available online 31 January 2023

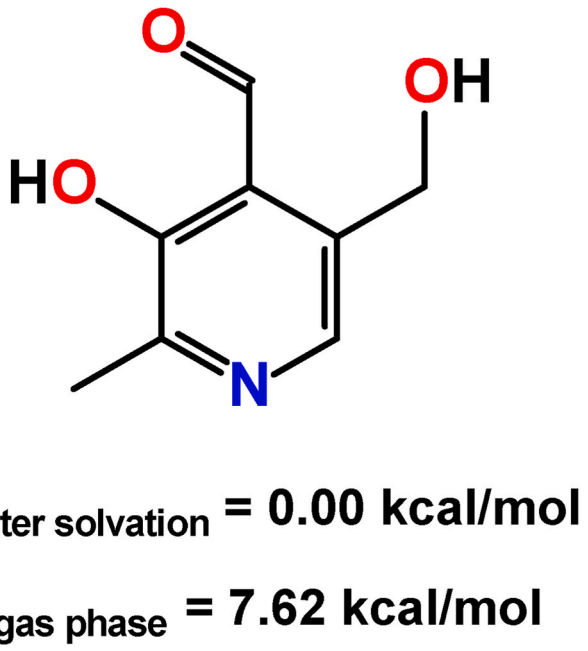

Fig. 1. Diagram of pyridoxal.

Table 1
Thermodynamic parameters of the optimized structure of pyridoxal in water, obtained using the DFT/B3LYP/6–311++G(d,p) method.

Self-consistent field energy (a.u.)	−590.868
Total energy (thermal) (kcal mol^{-1})	109.002
Electronic energy (thermal) (kcal mol^{-1})	0.000
Translational energy (thermal) (kcal mol^{-1})	0.889
Rotational energy (thermal) (kcal mol^{-1})	0.889
Vibrational energy (thermal) (kcal mol^{-1})	107.224
Total heat capacity (thermal) (cal mol^{-1} K^{-1})	42.152
Electronic heat capacity (thermal) (cal mol^{-1} K^{-1})	0.000
Translational heat capacity (thermal) (cal mol^{-1} K^{-1})	2.981
Rotational heat capacity (thermal) (cal mol^{-1} K^{-1})	2.981
Vibrational heat capacity (thermal) (cal mol^{-1} K^{-1})	36.191
Total entropy (thermal) (cal mol^{-1} K^{-1})	103.838
Electronic entropy (thermal) (cal mol^{-1} K^{-1})	0.000
Translational entropy (thermal) (cal mol^{-1} K^{-1})	41.248
Rotational entropy (thermal) (cal mol^{-1} K^{-1})	30.688
Vibrational entropy (thermal) (cal mol^{-1} K^{-1})	31.902
Zero-point vibrational energy (thermal) (kcal mol^{-1})	101.880
Rotational constants (GHz):	
A	1.32151
B	0.83224
C	0.53085

methyl)-2-methylisonicotinaldehyde (pyridoxal) (Fig. 1), which is known as one form of vitamin B_6 and is a forerunner of the Great Oxidation Event [30]. Pyridoxal was first synthesized in 1944 by Carl August Folkers, who also played a key role in determining its structure [31]. Furthermore, pyridoxal, which is a pyridine-based molecule, contains an aldehyde functionality as well as the hydroxyl group in the *ortho*-position, thus being a close analogue of salicylaldehyde. Notably, salicylaldehyde derived Schiff bases are of great interest and importance due to the *ortho*-OH group, bringing the imine and hydroxyl functionalities in close proximity, leading to a possible enol–keto tautomerization [32–39]. As a result, salicylaldehyde derived Schiff bases exhibit rich colour panel due to adopting different tautomeric forms. Thus, pyridoxal is an important precursor for an intriguing class of Schiff bases.

A comprehesive search through the Cambridge Structural Database (CSD) [40] did not reveal crystal structures for pyridoxal. However, the CSD contains a crystal structure of the hydrochloride salt of pyridoxal with the protonated pyridine ring [41]. Thus, it is of importance to reveal some structural features of pyridoxal. As such, we have performed the DFT-based computational studies to probe the most favorable structure of the title compound as well as to examine its electronic, optical, magnetic, reactivity and corrosion inhibition properties. Additionally, interaction of pyridoxal with some SARS-CoV-2 proteins and A42R Profilin-like protein from monkeypox was examined using molecular docking. Interaction of pyridoxal with nonstructural protein 15 (endoribonuclease) was further probed using the molecular dynamics simulation.

2. Experimental

2.1. DFT calculations

The optimized geometry of pyridoxal as well as vibration frequencies, nonlinear optical properties, highest occupied and lowest unoccupied molecular orbital (HOMO and LUMO, respectively) surfaces, and molecular electrostatic potential (MEP) surface were calculated without symmetry restrictions in water and gas phase with the GaussView 6.0 molecular visualization program [42] and Gaussian 09, Revision D.01 program package [43] using the DFT/B3LYP hybrid functional [44,45] and 6–311++G(d,p) [44,46] basis set. The Polarizable Continuum Model using the integral equation formalism variant (IEFPCM) was applied for calculations in water. The absorption and ^{1}H NMR spectra were simulated at the TD-DFT/B3LYP/6–311++G(d,p) and GIAO/B3LYP/6–311++G(2d,p) levels, respectively. The density-of-states (DOS) plot was calculated using the GaussSum 3.0 software [47,48].

2.2. Molecular docking

The optimized structure of pyridoxal in water was used for molecular docking studies with the applied SARS-CoV-2 proteins and A42R profilin-like protein from monkeypox virus Zaire-96-I-16 using AutoDock Vina [49,50]. The structures of proteins were subtracted from the RCSB PDB database [51], and were pretreated before docking, including water removing and inserting hydrogen atoms and missing residues and charges. The lowest binding energy conformers and 2D interactions were filtered from 10 top ranked poses. BIOVIA Discovery Studio 2020 [52] was utilized for visualization of the docked conformations and 3D target-ligand interactions.

2.3. In silico drug-likeness analysis

The SwissADME [53,54], BOILED-Egg [55] and ProTox-II [56,57] tools were applied to sudy ADMET properties of pyridoxal.

2.4. Molecular dynamics simulation

Molecular dynamics (MD) simulations of the pyridoxal complex with nonstructural protein 15 (endoribonuclease) were performed using a GROMACS-2020 software package (GNU, General Public License) [58].

Table 2
Selected bond lengths (Å), bond and dihedral angles (°) in the optimized structure of pyridoxal, obtained using the DFT/B3LYP/6–311++G(d,p) method.

Bond length					
C1–C2	1.418	C1–C6	1.502	C5–N	1.347
C2–C3	1.408	C3–C8	1.464	C2–O2	1.343
C3–C4	1.416	C4–C7	1.507	C7–O1	1.437
C4–C5	1.384	C1–N	1.327	C8–O3	1.231
Bond angle					
C1–C2–C3	119.59	C4–C3–C8	121.94	C1–C2–O2	117.75
C2–C1–C6	120.06	C5–C4–C7	119.92	C3–C2–O2	122.66
C2–C3–C4	118.40	C2–C1–N	120.71	C3–C8–O3	123.14
C2–C3–C8	119.66	C4–C5–N	123.92	C4–C7–O1	108.73
C3–C4–C5	117.45	C6–C1–N	119.23	C1–N–C5	119.92
C3–C4–C7	122.63				
Dihedral angle					
C1–C2–C3–C4	−0.37	C3–C2–C1–N	0.27	C5–C4–C7–O1	−115.51
C1–C2–C3–C8	179.12	C3–C4–C5–N	0.31	C6–C1–C2–O2	−0.01
C2–C3–C4–C5	0.10	C7–C4–C5–N	−179.93	C8–C3–C2–O2	−0.73
C2–C3–C4–C7	−179.66	C2–C3–C8–O3	1.16	C2–C1–N–C5	0.12
C3–C2–C1–C6	−179.86	C3–C4–C7–O1	64.24	C4–C5–N–C1	−0.43
C5–C4–C3–C8	−179.38	C4–C3–C2–O2	179.78	C6–C1–N–C5	−179.74
C7–C4–C3–C8	0.86	C4–C3–C8–O3	−179.36	N–C1–C2–O2	−179.88

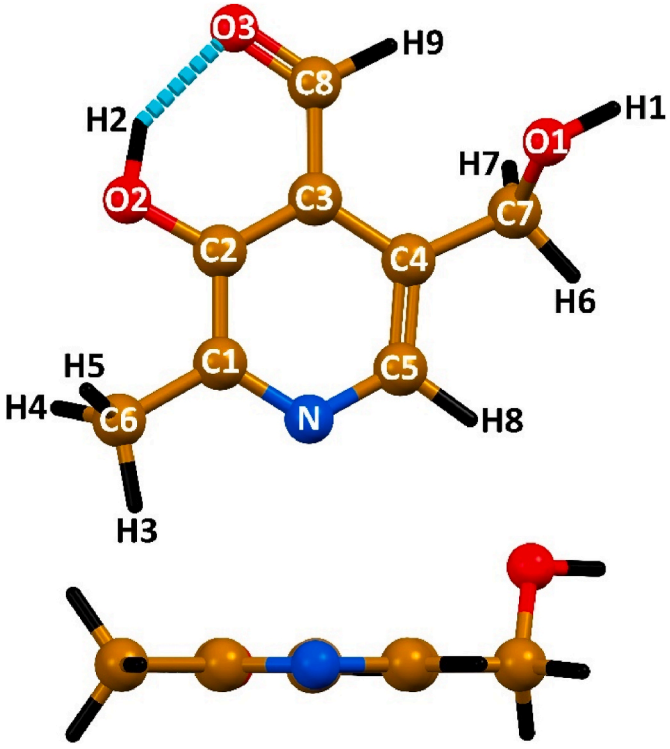

Fig. 2. Optimized structure of pyridoxal in water, obtained using the DFT/B3LYP/6–311++G(d,p) method.

Parameters such as root mean square deviation (RMSD), root mean square fluctuation (RMSF), radius of gyration (Rg), solvent accessible surface area (SASA) and intermolecular hydrogen bonds were evaluated. The related complex was prepared for MD using the CHARMm36 force field and equilibrated using the canonical (NVT) and isothermal-isobaric (NPT) ensembles. Transferable intermolecular potential with a three-points TIP3P was chosen to simulate MD in explicit solvation. The MD simulations were performed in the presence 0.15 M NaCl using the constant temperature (310 K) and pressure (1.0 bar). Approximate number of frames per simulation was 1000. The simulation time was set to 100 ns Trajectories were analyzed using the GROMACS tools.

3. Results and discussion

The structure of pyridoxal was examined using the DFT/B3LYP/6–311++G(d,p) method both in gas phase and water at 298.15 K. Calculations in water were performed as for the medium for physiological processes.

According to the DFT results, it was established that although the optimized structure of pyridoxal adopts almost the same geometry both in gas phase and in water, the optimized structure of pyridoxal is 7.62 kcal/mol more favorable under water solvation conditions in comparison to gas phase (Fig. 1). For the sake of brevity, we have further focused on the DFT results obtained for pyridoxal in water.

The calculated energies and thermodynamic parameters of pyridoxal in water are given in Table 1. The calculated C–C bond lengths within the pyridine ring vary from 1.384 Å to 1.418 Å, while the C–N bonds vary from 1.327 Å to 1.347 Å (Table 2). The exocyclic C–C bonds, formed with the methyl and methylene carbon atoms, are remarkably longer, and of 1.502 Å and 1.507 Å, respectively. However, the C–C bond, formed with the carbonyl carbon atom, is somewhat shorter (1.464 Å) due to conjugation of the carbonyl and pyridine π-systems. The C–O bond length of the carbonyl fragment is 1.231 Å, while the same bond formed by the methylene carbon atom is 1.437 Å, clearly

Table 3
Hydrogen bond lengths (Å) and angles (°), and aromaticity indexes of the pyridine and six-membered non-covalent rings in the optimized structure of pyridoxal in water, obtained using the DFT/B3LYP/6–311++G(d,p) method.

O–H···O	*d*(O–H)	*d*(H···O)	*d*(O···O)	∠(OHO)	Aromaticity index	
					pyridine	non-covalent ring
O2–H2···O3	0.986	1.731	2.606	145.92	0.967	0.753

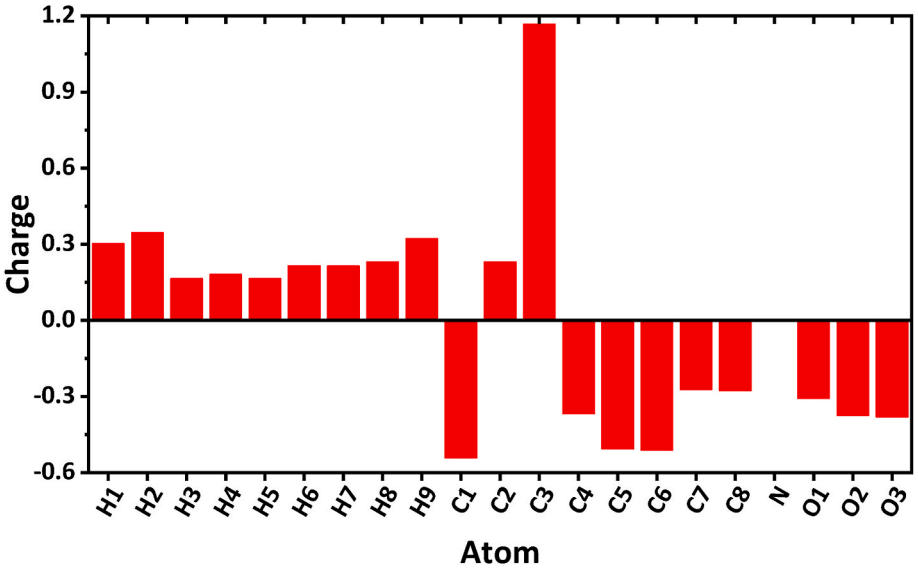

Fig. 3. Mulliken atomic charges in the optimized structure of pyridoxal in water, obtained using the DFT/B3LYP/6–311++G(d,p) method (see Fig. 2 for atoms labelling).

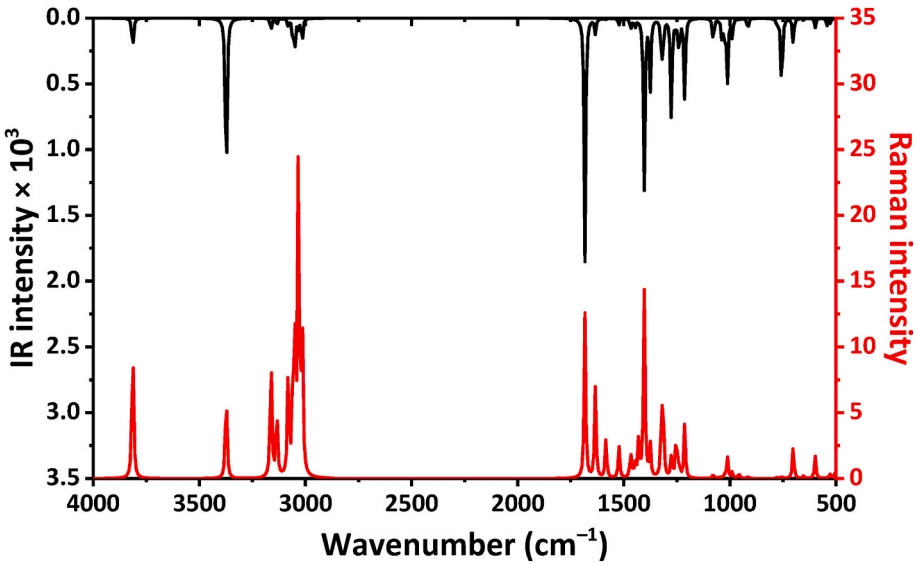

Fig. 4. The calculated IR (black) and Raman (red) spectra of pyridoxal in water, obtained using the DFT/B3LYP/6–311++G(d,p) method. (For interpretation of the references to colour in this figure legend, the reader is referred to the Web version of this article.)

indicating their double bond and single bond nature, respectively. Interestingly, the C–O bond formed by one of the pyridine carbon atoms is 1.343 Å due to partial double bond character. The bond angles formed by the pyridine atoms and carbonyl carbon atom vary from 117.45° to 123.92°, indicating their sp^2-hybridization, while the bond angle formed around the methylene carbon atom is 108.73°, which is typical for sp^3-hybridization (Table 2). As evidenced from the corresponding dihedral angles between the non-hydrogen atoms (Table 2), the structure of pyridoxal is planar with the C–O group, formed by the methylene carbon atom, being remarkably deviated (Fig. 2).

Notably, the optimized molecule of pyridoxal is stabilized by the hydrogen bond O2–H2···O3 with the formation of a six-membered pseudoaromatic ring (Fig. 2, Table 3) due to conjugation effects [59]. This leads to the so-called resonance-assisted hydrogen bonding [60]. We have calculated the aromaticity index for both the pyridine and hydrogen bonded rings of pyridoxal using the HOMHED approach [60], which revealed values of 0.753 and 0.967, respectively. Notably, the former value is very similar to those of furans and (is)oxazoles [60].

Analysis of the Mulliken atomic charges in the optimized structure of pyridoxal revelead that all the hydrogen atoms are positively charged

Table 4
Frontier molecular orbitals, gap value, descriptors and charge transfer parameters for the optimized structure of pyridoxal in water, obtained using the DFT/B3LYP/6–311++G(d,p) method.

E_{HOMO} (eV)	−6.86244
E_{LUMO} (eV)	−2.74617
$\Delta E_{LUMO\ -\ HOMO} = E_{LUMO} - E_{HOMO}$ (eV)	4.11627
Ionization energy, $I = -E_{HOMO}$ (eV)	6.86244
Electron affinity, $A = -E_{LUMO}$ (eV)	2.74617
Electronegativity, $\chi = (I + A)/2$ (eV)	4.80431
Chemical potential, $\mu = -\chi$ (eV)	−4.80431
Global chemical hardness, $\eta = (I - A)/2$ (eV)	2.05814
Global chemical softness, $S = 1/(2\eta)$ (eV^{-1})	0.24294
Global electrophilicity index, $\omega = \mu^2/(2\eta)$ (eV)	5.60735
Maximum additional electric charge, $\Delta N_{max} = -\mu/\eta$	2.33430
Molecule-to-metal electron charge transfer, $\Delta N_1 = (\Phi - \chi)/\eta$:	
Ti	−0.23
Fe	−0.15
Zr	−0.37
Co	0.10
Cu	−0.07
Cr	−0.15
Ni	0.17
Mn	−0.34
Mo	−0.10
Zn	−0.23
Al	−0.25
W	−0.12
Ag	−0.26
Total negative charge, TNC (e)	−3.53781

with the highest values corresponding to the hydroxyl and aldehyde hydrogen atoms (Fig. 3). Of non-hydrogen atoms, the C2 and C3 carbon atoms are exclusively positively charged, while the charge of the pyridine nitrogen atom is almost zero (Fig. 3). The C1, C5 and C6 carbon atoms are the most negatively charged atoms in the discussed structure (Fig. 3). Finally, all the oxygen atoms are also negatively charged (Fig. 3).

Vibrational analysis revealed 57 normal modes in the IR and Raman spectra, exclusively with positive wavenumbers, since the molecule of pyridoxal is constructed from 21 atoms (Fig. 4). Both spectra exhibit two bands at 3373 and 3814 cm^{-1}, corresponding to the stretching modes of the O2–H2 and O1–H1 groups, respectively (Fig. 4). The spectra also contain a set of bands at 2960–3200 cm^{-1} for the C–H stretching. The carbonyl functionality was shown as an intense band at 1683 cm^{-1}.

According to the DFT calculations, the energies of the HOMO and LUMO for the optimized structure of pyridoxal in water are −6.86244 and −2.74617 eV, respectively, with the HOMO–LUMO energy gap of 4.11627 eV (Table 4). The HOMO is spread over the whole molecule except for the N, H1, H3, H9 and C7–H6 fragments (Fig. 5). The LUMO is also distributed almost the whole molecule except for the methyl and methylene fragments, H1, H2 and H8 atoms (Fig. 5). The density-of-states (DOS) plot of the optimized structure of pyridoxal in water is shown in Fig. 6.

The HOMO and LUMO values are of importance to estimate corrosion inhibition properties of a compound [61–65]. This becomes even more crucial considering metal-based biomedical implants [66–68]. In this work we have also probed potential corrosion inhibition properties of the optimized structure of pyridoxal in water towards a series of metals, which are prominent components of biomedical implants (Table 4) [68]. As such, we have used the most reliable equation, which includes the so-called work function (Φ) [69], to calculate electron carge transfer (Table 4) [65]. According to the obtained results, it was

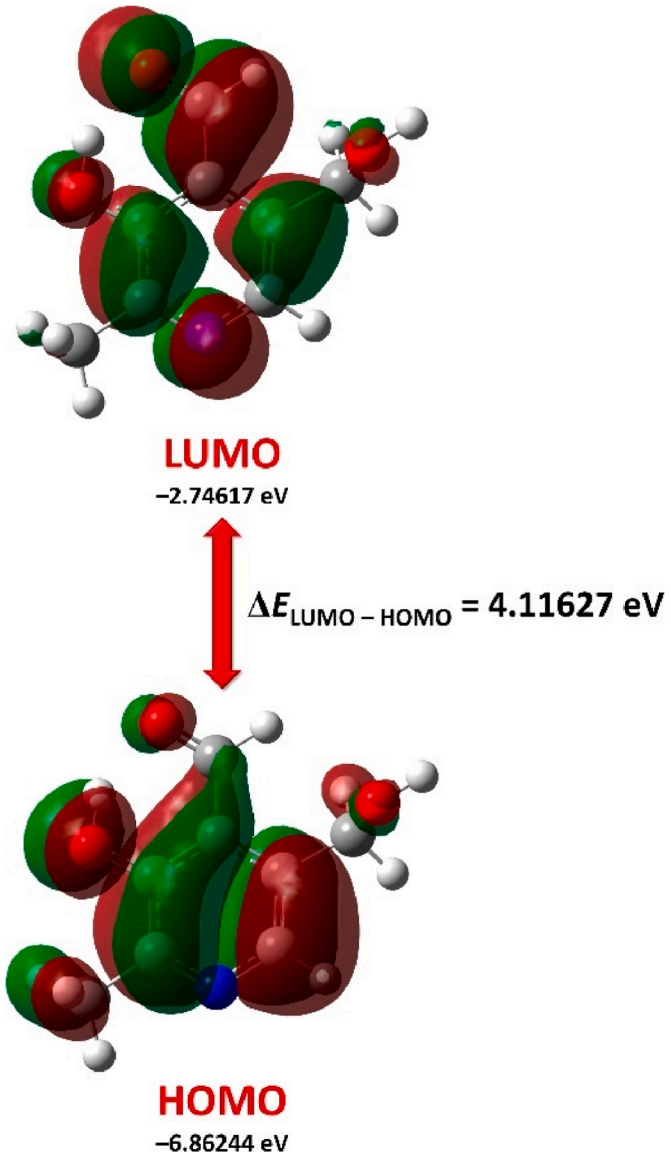

Fig. 5. The HOMO and LUMO isosurfaces of the ground state of the optimized structure of pyridoxal in water, obtained using the DFT/B3LYP/6–311++G(d,p) method.

revealed electron charge transfer from pyridoxal to the surface of Ni and Co (Table 4). Total negative charge (TNC) value is a parameter to indicate an adsorption of a molecule-inhibitor onto a metal surface and defined as a sum of negative Mulliken charges of atoms. As lower the absolute value of TNC as better a molecule will donate electrons to the metal surface, thus exhibiting better corrosion inhibition efficienct. For pyridoxal, the TNC value is about −3.54 electrons (Table 4).

We have also examined the molecular electrostatic potential (MEP) surface of the optimized structure of pyridoxal in water to reveal nucleophilic and electrophilic regions of a molecule. As a result, oxygen and nitrogen atoms were established to be the most distinguished nucleophilic stes (red colour), while the three hydrogen atoms of the CH_2OH group were highlighted as the most pronounced electrophilic

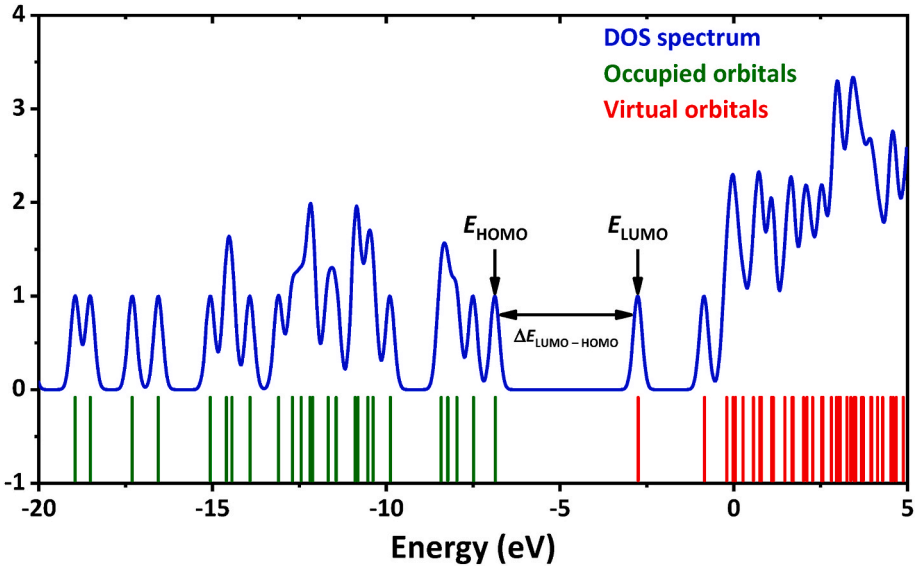

Fig. 6. The DOS plot for the ground state of the optimized structure of pyridoxal in water, obtained using the DFT/B3LYP/6–311++G(d,p) method.

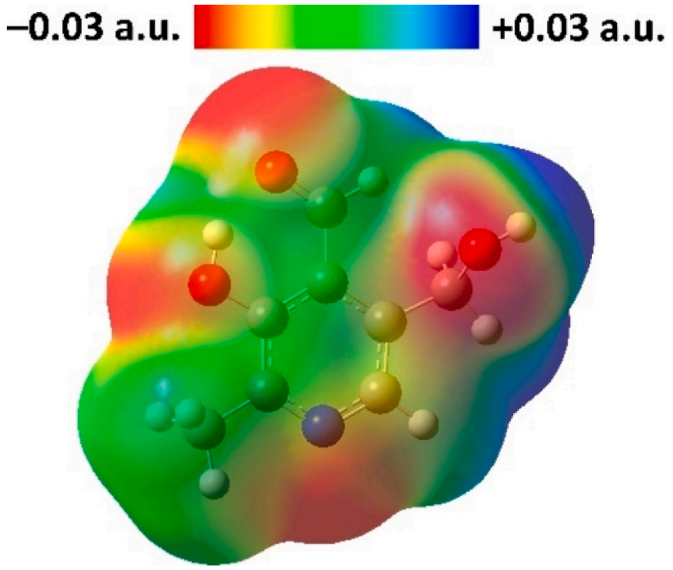

Fig. 7. View of the molecular electrostatic potential surface of the ground state of the optimized structure of pyridoxal in water, obtained using the DFT/B3LYP/6–311++G(d,p) method.

sites (blue colour) (Fig. 7).

The theoretical absorption spectrum of the optimized structure of pyridoxal in water contains an intense narrow band at 175 nm, accompanied with a broad band of about half intensity at ~215 nm, and a low intense broad band at 345 nm (Fig. 8). The main transitions responsible for the observed bands are given in Table 5.

According to the ionization potential and the electron affinity value, the optimized structure of pyridoxal in water exhibits moderate electron-donor and good electron-acceptor properties (Table 4) [70]. Further, as evidenced from the relatively low electronegativity value, pyridoxal is a good electron attractor, which is additionally supported by the corresponding chemical potential value (Table 4). Values of the chemical hardness and chemical softness indicate that the optimized structure of pyridoxal in water tends to exchange its electron cloud with surrounding environment (Table 4) [70]. The electrophilicity index value of the pyridoxal molecule is of about 5.61 eV, which is in the range for strong electrophiles [70,71]. The corresponding ΔN_{max} value indicate that pyridoxal can accept about 2.33 electrons (Table 4).

The calculated ^{1}H NMR spectrum (Table 6) of the reported structure contains signals for the methyl and methylene hydrogen atoms at 2.34–2.67 and 4.72–5.37 ppm, respectively, while the signals for the pyridine and aldehyde protons were calculated at 8.22 and 10.81 ppm, respectively. Finally, the signal for the CH_2OH hydroxyl hydrogen atom was shown at 1.33 ppm, while the signal of the hydrogen atom of the other hydroxyl group was revealed at 12.11 ppm.

In this work, we have also probed the optimized structure of pyridoxal in water for its potential NLO properties. Firstly, the calculated dipole moment was found 4.7292 Debye with the μ_x component being the main contributor, followed by the μ_z and μ_y components, respectively (Table 7). Notably, polarizability (α) and first-order hyperpolarizability (β) values for pyridoxal were calculated to be about 6.1 and 4.0 times higher compared to the same parameters for urea (Table 7). The latter compound is considered as a reference for comparison of the NLO properties of molecules [72].

According to the SwissADME [53,54] bioavailability radar and ProTox-II [56,57], pyridoxal is favoured in all the considered six parameters and is attributed to a fourth class of toxicity (Fig. 9). Further, one of the efficient approaches to examine molecues for the human blood-brain barrier (BBB) penetration and gastrointestinal absorption (GIA) is the BOILED-Egg method, which is derived from lipohilicity and polarity (Fig. 9) [55]. As such, points in the Egg's yolk and white correspond to molecules, which were predicted to passively permeate through the BBB and passively absorbed by the gastrointestinal tract, respectively. Furthermore, molecules found to be effluated (PGP+) and not to be effluated (PGP–) from the central nervous system by the P-glycoprotein are shown as blue and red dots, respectively. Thus, pyridoxal was predicted to possess negative BBB penetration and

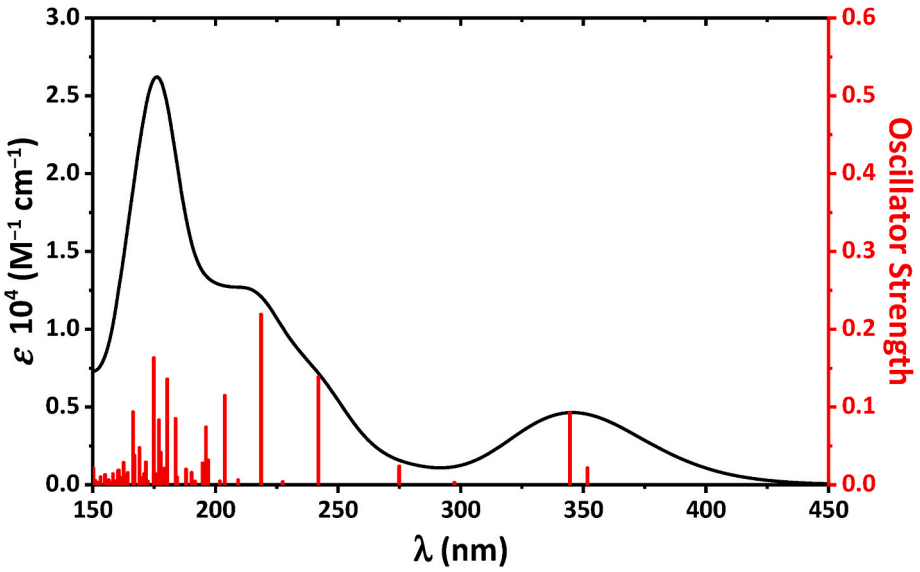

Fig. 8. The theoretical absorption spectrum of the optimized structure of pyridoxal in water, obtained using the TD-DFT/B3LYP/6–311++G(d,p) method.

Table 5
Selected values for the theoretical absorption spectrum (Fig. 8) for the optimized structure of pyridoxal in water, obtained using the TD-DFT/B3LYP/6–311++G(d,p) method.

λ_{max} (nm)	Osc. strength	Transition	λ_{max} (nm)	Osc. strength	Transition
351.67	0.0219	HOMO–1 → LUMO (68.5%)	180.39	0.1359	HOMO–7 → LUMO (13.3%)
		HOMO → LUMO (22.5%)			HOMO–6 → LUMO (9.6%)
344.53	0.0930	HOMO–1 → LUMO (20.2%)			HOMO–4 → LUMO+1 (13.3%)
		HOMO → LUMO (75.1%)			HOMO → LUMO+6 (25.4%)
274.92	0.0240	HOMO–4 → LUMO (15.0%)			HOMO → LUMO+7 (9.3%)
		HOMO–2 → LUMO (75.9%)	176.97	0.0832	HOMO–3 → LUMO+2 (10.0%)
241.96	0.1388	HOMO–4 → LUMO (71.2%)			HOMO–1 → LUMO+5 (69.0%)
		HOMO–3 → LUMO (14.8%)	174.90	0.1631	HOMO–7 → LUMO (14.2%)
218.60	0.2193	HOMO → LUMO+1 (80.8%)			HOMO–6 → LUMO (19.0%)
203.80	0.1149	HOMO–2 → LUMO+1 (19.8%)			HOMO–4 → LUMO+1 (14.4%)
		HOMO → LUMO+3 (51.8%)			HOMO → LUMO+8 (15.0%)
		HOMO → LUMO+4 (11.8%)	169.01	0.0480	HOMO–2 → LUMO+4 (23.4%)
196.13	0.0743	HOMO–3 → LUMO+1 (19.4%)			HOMO → LUMO+9 (22.9%)
		HOMO–2 → LUMO+1 (47.4%)			HOMO → LUMO+10 (20.5%)
		HOMO–1 → LUMO+3 (12.4%)	166.37	0.0937	HOMO–9 → LUMO (79.8%)
183.73	0.0852	HOMO–4 → LUMO+1 (22.6%)			
		HOMO → LUMO+6 (56.8%)			

Table 6
Signals for the calculated ^{1}H NMR spectrum of the ground state of the optimized structure of pyridoxal in water, obtained using the DFT/GIAO/B3LYP/6–311++G(2d,p) method (see Fig. 2 for atoms labelling).

δ (ppm)	Hydrogen	δ (ppm)	Hydrogen
1.33	H1	5.37	H7
2.34	H3	8.22	H8
2.67	H4 + H5	10.81	H9
4.72	H6	12.11	H2

positive GIA property with the PGP– effect (Fig. 9). Additionally, as evidenced from the Toxicity Model Report, pyridoxal was revealed to be nontotoxic (Fig. 9).

Finally, pyridoxal was examined as a potentional inhibitor toward a set of SARS-CoV-2 proteins (Table 8) using in silico molecular docking. Nowadays, this method is popular to probe interaction of a biomolecule with a ligand (small molecule) to design and discover new drugs [73–75], thus being efficient to save time and money.

According to the docking analysis results, pyridoxal was found to be active against all the applied SARS-CoV-2 proteins with the best binding affinity with nonstructural protein 15 (endoribonuclease) (Fig. 10, Table 8). Complex of pyridoxal with this protein is defined by four conventional hydrogen bonds with LYS71, ASP297, ASP273 and SER274; two carbon hydrogen bonds with SER274 and THR275; and one π···alkyl interacion with LYS277 (Fig. 10, Table 8). The title compound also interacts with Omicron Spike protein with even a bettter binding affinity (Table 8) through three conventional hydrogen bonds with LEU998, GLN1002 and GLY996; one carbon hydrogen bond with SER1000; and one π···π stacked interaction with PHE756 (Fig. 10, Table 9).

Nowadays, besides the COVID-19 pandemic, the other infectious viral disease, namely monkeypox, is continuously rising [76]. With this in mind, we have also probed pyridoxal as a potential inhibitor towards one of the monkeypox protein, viz. A42R Profilin-like protein from monkeypox (strain Zaire-96-I-16). According to the docking analysis results, pyridoxal was found to be also active against this protein (Table 8). Complexation of the ligand with the monkeypox protein is characterized by three conventional hydrogen bonds with ARG115, ARG122 and ASP123; one π···π T-shaped interaction with TYR118; and one π···alkyl interaction with ARG119 (Fig. 10, Table 9).

Table 7
Nonlinear optical (NLO) parameters for the ground state of the optimized structure of pyridoxal in water and urea, obtained using the DFT/B3LYP/6–311++G(d,p) method. [a]

Parameter	pyridoxal	Urea [72]	Parameter	pyridoxal	Urea [72]
μ_x (Debye)	3.9969		β_{xxx} (a.u.)	72.4069	
μ_y (Debye)	−1.4929		β_{yyy} (a.u.)	−11.5977	
μ_z (Debye)	−2.0400		β_{zzz} (a.u.)	0.1910	
μ_D (Debye)	4.7292		β_{xyy} (a.u.)	16.5547	
α_{xx} (a.u.)	195.761		β_{xxy} (a.u.)	−8.8479	
α_{yy} (a.u.)	181.916		β_{xxz} (a.u.)	−7.3672	
α_{zz} (a.u.)	92.229		β_{xzz} (a.u.)	−0.7627	
α_{xy} (a.u.)	2.442		β_{yzz} (a.u.)	8.0279	
α_{xz} (a.u.)	−7.560		β_{yyz} (a.u.)	−0.4773	
α_{yz} (a.u.)	2.803		β_{xyz} (a.u.)	2.8401	
α (a.u.)	156.635		β (a.u.)	89.3970	
α (esu)	23.2134×10^{-24}	3.8312×10^{-24}	β (esu)	0.7723×10^{-30}	0.1947×10^{-30}
$\alpha_{pyridoxal}/\alpha_{urea}$	6.1		$\beta_{pyridoxal}/\beta_{urea}$	4.0	
Δα (a.u.)	98.438				
Δα (esu)	14.5885×10^{-24}				

[a] For α 1 a.u. = 0.1482×10^{-24} esu, [a]for β 1 a.u. = 8.6393×10^{-33} esu.

We have additionaly applied molecular dynamics (MD) simulations of 100 ns at 310 K to evaluate interactions in the pyridoxal complex with nonstructural protein 15 (endoribonuclease), which showed the most significant docking score within the applied nonstructural proteins. Particularly, the complex displayed an RMSD value between 0.160 nm and 0.368 nm, which is in the acceptable range (Fig. 11). The RMSF value for the same complex is mainly below 3.0 nm with the strongest fluctuations observed for the residue positions 37, 265 and 347 (Fig. 11). Radius of gyration (Rg) values for this complex form a relatively stable profile from 2.313 nm to 2.439 nm (Fig. 11). The SASA profile was computed to estimate interaction between the complex of nonstructural protein 15 (endoribonuclease) with pyridoxal and solvents. It was found that the binding of pyridoxal to nonstructural protein 15 (endoribonuclease) did not decrease the interactions of the target protein with the solvent molecules and the stability of the protein (Fig. 11). During the 100 ns simulation time, the average SASA was calculated as 179.194 nm^2. It was also observed that the complex forms 1 intermolecular hydrogen bond during almost the whole simulation time; 2 intermolecular hydrogen bonds up to about 20 ns, at about 79–82 and 87–92 ns; 3 intermolecular hydrogen bonds up to about 20 ns and at 98 ns; and 4 intermolecular hydrogen bonds at about 6–18 ns (Fig. 11).

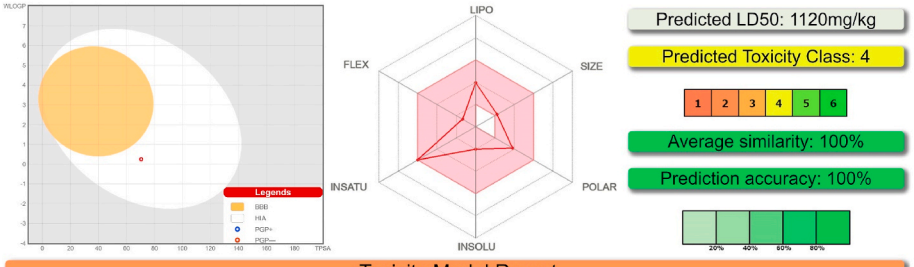

Toxicity Model Report

Classification	Target	Prediction	Probability
Organ toxicity	Hepatotoxicity	Inactive	0.71
Toxicity end points	Carcinogenicity	Inactive	0.63
Toxicity end points	Immunotoxicity	Inactive	0.93
Toxicity end points	Mutagenicity	Inactive	0.77
Toxicity end points	Cytotoxicity	Inactive	0.81
Tox21-Nuclear receptor signalling pathways	Aryl hydrocarbon Receptor (AhR)	Inactive	0.94
Tox21-Nuclear receptor signalling pathways	Androgen Receptor (AR)	Inactive	0.99
Tox21-Nuclear receptor signalling pathways	Androgen Receptor Ligand Binding Domain (AR-LBD)	Inactive	1.0
Tox21-Nuclear receptor signalling pathways	Aromatase	Inactive	0.99
Tox21-Nuclear receptor signalling pathways	Estrogen Receptor Alpha (ER)	Inactive	0.98
Tox21-Nuclear receptor signalling pathways	Estrogen Receptor Ligand Binding Domain (ER-LBD)	Inactive	0.99
Tox21-Nuclear receptor signalling pathways	Peroxisome Proliferator Activated Receptor Gamma (PPAR-Gamma)	Inactive	0.99
Tox21-Stress response pathways	Nuclear factor (erythroid-derived 2)-like 2/antioxidant responsive element (nrf2/ARE)	Inactive	0.99
Tox21-Stress response pathways	Heat shock factor response element (HSE)	Inactive	0.99
Tox21-Stress response pathways	Mitochondrial Membrane Potential (MMP)	Inactive	0.96
Tox21-Stress response pathways	Phosphoprotein (Tumor Supressor) p53	Inactive	0.99
Tox21-Stress response pathways	ATPase family AAA domain-containing protein 5 (ATAD5)	Inactive	0.99

Fig. 9. BOILED-Egg model (top-left), the bioavailability radar (the coloured zone of the radar is the suitable physicochemical space for oral bioavailability of pyridoxal) within the domain borders of ADME properties, calculated by SwissADME (top-middle), and toxicity results, calculated by ProTox-II (top-right and bottom), of pyridoxal.

Table 8
The best poses of pyridoxal inside the binding sites of the listed proteins.

Protein	PDB code	Binding energy (kcal/mol)
Main protease (Mpro)	6LU7	−4.8(1)
Papain-like protease (PLpro)	6WUU	−5.7(1)
Nonstructural protein 3 (nsp3_range 207–379-AMP)	6W6Y	−4.9(1)
Nonstructural protein 3 (nsp3_range 207–379-MES)	6W6Y	−6.0(0)
RdRp-RNA	7BV2	−5.7(0)
Nonstructural protein 14 (N7-MTase)	5C8S	−5.1(0)
Nonstructural protein 15 (endoribonuclease)	6WLC	**−6.1(0)**
Nonstructural protein 16 (GTA site)	6WVN	−5.9(0)
Nonstructural protein 16 (MGP site)	6WVN	−5.1)0)
Nonstructural protein 16 (SAM site)	6WVN	−5.9(0)
Spike protein, RBD (native)	6M0J	−5.0(0)
Spike protein, RBD (mutated)	6M0J	−5.0(0)
Omicron (strain B.1.1.529) Spike protein	7QO7	**−6.4(0)**
A42R Profilin-like protein from monkeypox (strain Zaire-96-I-16)	4QWO	**−5.7(1)**

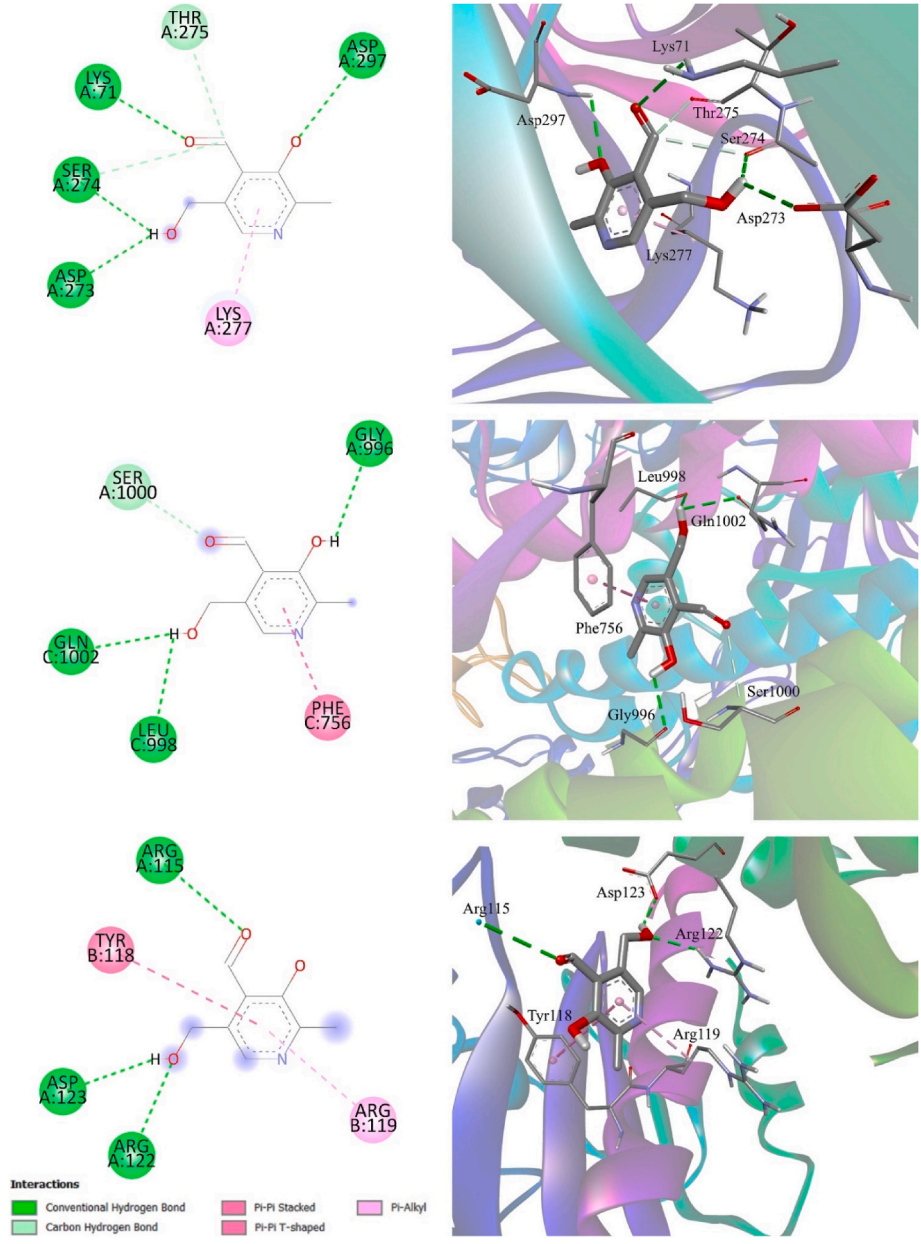

Fig. 10. 2D (left) and 3D (right) views on the interaction of pyridoxal with (from top to bottom) nonstructural protein 15 (endoribonuclease), Omicron (strain B.1.1.529) Spike protein and A42R Profilin-like protein from monkeypox (strain Zaire-96-I-16).

Table 9
Parameters of interaction of pyridoxal with nonstructural protein 15 (endoribonuclease), Omicron (strain B.1.1.529) Spike protein and A42R Profilin-like protein from monkeypox (strain Zaire-96-I-16).

Interaction	Distance (Å)	Bonding	Bonding type
Nonstructural protein 15 (endoribonuclease)–pyridoxal			
A:LYS71:HZ3 - :pyridoxal:O	2.77933	Hydrogen Bond	Conventional Hydrogen Bond
A:ASP297:HN - :pyridoxal:O	2.69781	Hydrogen Bond	Conventional Hydrogen Bond
:pyridoxal:H - A:ASP273:OD1	2.47842	Hydrogen Bond	Conventional Hydrogen Bond
:pyridoxal:H - A:SER274:O	2.47502	Hydrogen Bond	Conventional Hydrogen Bond
:pyridoxal:C - A:SER274:O	3.51838	Hydrogen Bond	Carbon Hydrogen Bond
:pyridoxal:C - A:THR275:O	3.33131	Hydrogen Bond	Carbon Hydrogen Bond
:pyridoxal - A:LYS277	3.91533	Hydrophobic	π···Alkyl
Omicron (strain B.1.1.529) Spike protein–pyridoxal			
:pyridoxal:H–C:LEU998:O	2.83317	Hydrogen Bond	Conventional Hydrogen Bond
:pyridoxal:H–C:GLN1002:OE1	2.76388	Hydrogen Bond	Conventional Hydrogen Bond
:pyridoxal:H - A:GLY996:O	2.67708	Hydrogen Bond	Conventional Hydrogen Bond
A:SER1000:CA - :pyridoxal:O	3.58345	Hydrogen Bond	Carbon Hydrogen Bond
C:PHE756 - :pyridoxal	3.86152	Hydrophobic	π···π Stacked
A42R Profilin-like protein from monkeypox (strain Zaire-96-I-16)–pyridoxal			
A:ARG115:HE:B - :pyridoxal:O	2.87226	Hydrogen Bond	Conventional Hydrogen Bond
A:ARG122:HH11 - :pyridoxal:O	2.37859	Hydrogen Bond	Conventional Hydrogen Bond
:pyridoxal:H - A:ASP123:OD1	2.16346	Hydrogen Bond	Conventional Hydrogen Bond
B:TYR118 - :pyridoxal	5.44035	Hydrophobic	π···π T-shaped
:pyridoxal - B:ARG119	4.68507	Hydrophobic	π···Alkyl

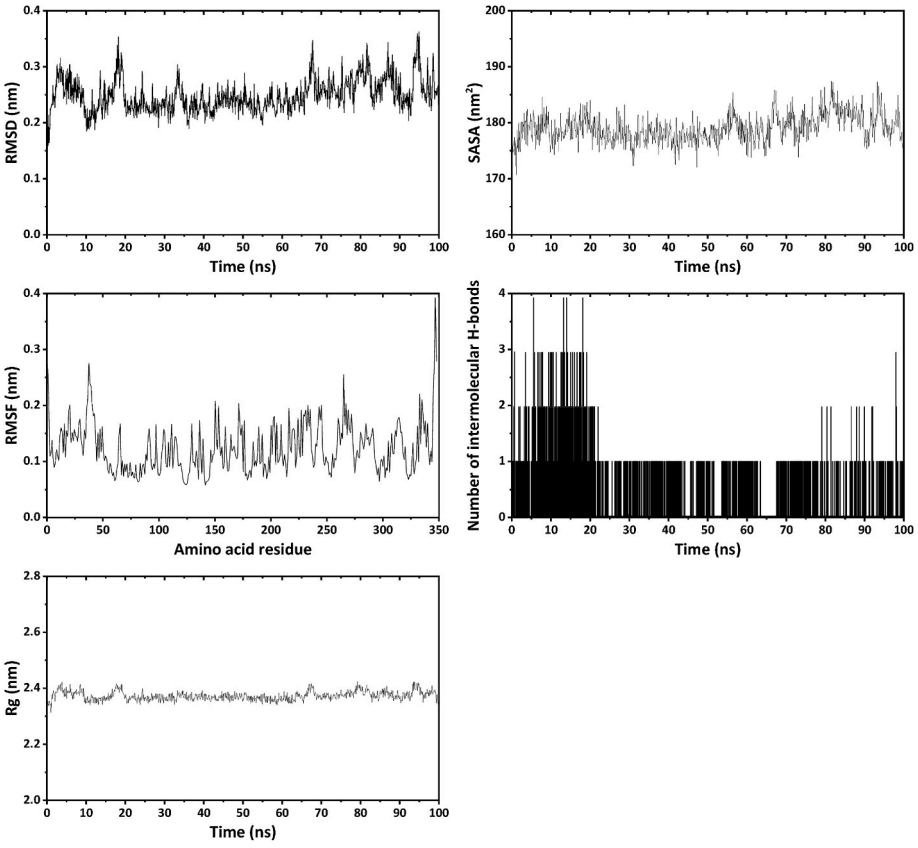

Fig. 11. RMSD, RMSF, Rg, SASA and intermolecular hydrogen bonds analysis profles of the nonstructural protein 15 (endoribonuclease)–pyridoxal complex.

4. Conclusions

To sum up, a detailed computational analysis of pyridoxal both under water solvation and in gas phase are reported. The structure, optical and electronic properties were revealed by the DFT/B3LYP/6–311++G(d,p) calculations. It was established that although the optimized structure of pyridoxal adopts almost the same geometry both in gas phase and in water, the optimized structure of pyridoxal is 7.62 kcal/mol more favorable under water solvation conditions.

The global chemical reactivity descriptors of the optimized structure of pyridoxal in water were also calculated, which allowed to reveal its electron accepting and donating abilities. Furthermore, the molecule of pyridoxal was found to be of potential interest for NLO since its polarizability and first-order hyperpolarizability parameters are superior to those of urea, which is considered as a reference for comparison of the NLO properties of molecules.

Some biological properties of the title compound were evaluated using a set of on-line tools, which revealed that pyridoxal exhibits the

negative human blood-brain barrier penetration and positive gastrointestinal absorption property. Furthermore, the molecule of pyridoxal was predicted not to be effluated from the central nervous system by the P-glycoprotein.

According to the molecular docking results it was established that pyridoxal is active against all the applied SARS-CoV-2 and monkeypox proteins with the best binding affinity with nonstructural protein 15 (endoribonuclease). The title compound also interacts with Omicron Spike protein with even a higher efficiency. Pyridoxal was found to be also active against the studied monkeypox protein. Based on molecular dynamics simulation data, nonstructural protein 15 (endoribonuclease) was revealed to form a stable complex with pyridoxal.

Declaration of competing interest

There are no conflicts to declare.

Acknowledgments

The numerical calculations were partially performed at TUBITAK ULAKBIM, High Performance and Grid Computing Center (TRUBA resources).

References

[1] M. Baumann, I.R. Baxendale, An overview of the synthesis routes to the best selling drugs containing 6-membered heterocycles, Beilstein J. Org. Chem. 9 (2013) 2265–2319.
[2] R.D. Taylor, M. MacCoss, A.D. Lawson, Rings in drugs, J. Med. Chem. 57 (2014) 5845–5859.
[3] H. Liu, S. Long, K.P. Rakesh, G.F. Zha, Structure-activity relationships (SAR) of triazine derivatives: promising antimicrobial agents, Eur. J. Med. Chem. 185 (2020), 111804.
[4] A. Morandini, E. Spadati, B. Leonetti, R. Sole, V. Gatto, F. Rizzolio, V. Beghetto, Sustainable triazine-derived quaternary ammonium salts as antimicrobial agents, RSC Adv. 11 (2021) 28092–28096.
[5] Y. Ling, Z.-Y. Hao, D. Liang, C.-L. Zhang, Y.-F. Liu, Y. Wang, The expanding role of pyridine and dihydropyridine scaffolds in drug design, Drug Des. Dev. Ther. 15 (2021) 4289–4338.
[6] M. Marinescu, C.-V. Popa, Pyridine compounds with antimicrobial and antiviral activities, Int. J. Mol. Sci. 23 (2022) 5659.
[7] A. Keeley, P. Ábrányi-Balogh, M. Hrast, T. Imre, J. Ilaš, S. Gobec, G.M. Keserű, Heterocyclic electrophiles as new MurA inhibitors, Arch. Pharm. 351 (2018), 1800184.
[8] A. Keeley, P. Ábrányi-Balogh, G.M. Keserű, Design and characterization of a heterocyclic electrophilic fragment library for the discovery of cysteine-targeted covalent inhibitors, MedChemComm 10 (2019) 263–267.
[9] Available online https://covid19.who.int/. (Accessed 10 February 2023).
[10] M. Negi, P.A. Chawla, A. Faruk, V. Chawla, Role of heterocyclic compounds in SARS and SARS CoV-2 pandemic, Bioorg. Chem. 104 (2020), 104315.
[11] D.A. Safin, Y. Xu, I. Korobkov, D.L. Bryce, M. Murugesu, Renaissance of the coordination chemistry of 2,4,6-tris(2-pyrimidyl)-1,3,5-triazine (TPymT). Part I: first crystal structure of a TPymT complex with a d-metal cation, CrystEngComm 15 (2013) 10419–10422.
[12] D.A. Safin, K. Burgess, I. Korobkov, D.L. Bryce, M. Murugesu, Renaissance of the coordination chemistry of 2,4,6-tris(2-pyrimidyl)-1,3,5-triazine (TPymT). Part II: new insights into the reaction of TPymT with $Pb(NO_3)_2$, CrystEngComm 16 (2014) 3466–3469.
[13] D.A. Safin, N.A. Tumanov, A.A. Leitch, J.L. Brusso, Y. Filinchuk, M. Murugesu, Elucidating the elusive crystal structure of 2,4,6-tris(2-pyrimidyl)-1,3,5-triazine, CrystEngComm 17 (2015) 2190–2195.
[14] D.A. Safin, R.J. Holmberg, K.M.N. Burgess, K. Robeyns, D.L. Bryce, M. Murugesu, Hybrid material constructed from $Hg(NCS)_2$ and 2,4,6-Tris(2-pyrimidyl)-1,3,5-triazine (TPymT): coordination of TPymT in a 2,2′-bipyridine-like mode, Eur. J. Inorg. Chem. (2015) 441–446.
[15] D.A. Safin, A. Pialat, I. Korobkov, M. Murugesu, Unprecedented trinuclear Ag^I complex with 2,4,6-Tris(2-pyrimidyl)-1,3,5-triazine as an efficient catalyst for the aziridination of olefins, Chem. Eur J. 16 (2015) 6144–6149.
[16] D.A. Safin, A. Pialat, A. Leitch, N.A. Tumanov, I. Korobkov, Y. Filinchuk, J. L. Brusso, M. Murugesu, Anion-induced Ag^I self-assemblies with electron deficient aromatic ligands: anion–π-system interactions as a driving force for templated coordination networks, Chem. Commun. 51 (2015) 9547–9550.
[17] D.A. Safin, P.M.J. Szell, A. Keller, I. Korobkov, D.L. Bryce, M. Murugesu, Interaction of 2,4,6-tris(2-pyrimidyl)-1,3,5-triazine (TPymT) with CoX_2 (X = Cl, Br) in water: trapping of new self-assembled water–chloride/bromide clusters in a $[Co(bpca)_2]^+$ host (bpca = bis(2-pyrimidylcarbonyl)amidate anion), New J. Chem. 39 (2015) 7147–7152.
[18] D.A. Safin, J.M. Frost, M. Murugesu, The renaissance of 2,4,6-tris(2-pyrimidyl)-1,3,5-triazine (TPymT) coordination chemistry, Dalton Trans. 44 (2015) 20287–20294.
[19] B. Ay, O. Şahin, B. Saygıdeğer Demir, Y. Saygideger, J.M. López-de-Luzuriaga, G. Mahmoudi, D.A. Safin, Antitumor effects of novel nickel–hydrazone complexes in lung cancer cells, New J. Chem. 44 (2020) 9064–9072.
[20] L.E. Alkhimova, M.G. Babashkina, D.A. Safin, α-Aminophosphonates 4-$XC_6H_4$5–NH–CH(4-BrC_6H_4)–P(O)$(OiPr)_2$ (X = H, Br, MeO): crystal structures, Hirshfeld surface analysis, computational studies and in silico molecular docking with the SARS-CoV-2 proteins, Tetrahedron 97 (2021), 132376.
[21] A.A. Shiryaev, A.N. Goncharenko, T.M. Burkhanova, L.A. Alkhimova, M. G. Babashkina, R. Chandrasekaran, D.A. Safin, A chiral (1*R*,2*R*)-*N*,*N*′-bis-(salicylidene)-1,2-diphenyl-1,2-ethanediamine Schiff base dye: synthesis, crystal structure, Hirshfeld surface analysis, computational study, photophysical properties and in silico antifungal activity, J. Iran. Chem. Soc. 18 (2021) 2897–2911.
[22] M.G. Babashkina, A. Frontera, A.V. Kertman, Y. Saygideger, S. Murugavel, D. A. Safin, Favipiravir: insight into the crystal structure, Hirshfeld surface analysis and computational study, J. Iran. Chem. Soc. 19 (2022) 85–94.
[23] L.E. Alkhimova, M.G. Babashkina, D.A. Safin, Computational analysis of aspirin, J. Mol. Struct. 1251 (2022), 131975.
[24] T.M. Burkhanova, M.G. Babashkina, T. Taskin-Tok, A.V. Sharov, D.A. Safin, Naphthalene-based bis-N-salicylidene aniline dyes: crystal structures, Hirshfeld surface analysis, computational study and molecular docking with the SARS-CoV-2, J. Iran. Chem. Soc. 19 (2022) 1979–1991.
[25] L.E. Alkhimova, T.M. Burkhanova, M.G. Babashkina, D.A. Safin, A readily available structural analogue of integrastatins A and B: insight into the crystal structure, Hirshfeld surface analysis and computational study, Tetrahedron 109 (2022), 132671.
[26] A.V. Sharov, T.M. Burkhanova, T. Taskın Tok, M.G. Babashkina, D.A. Safin, Computational analysis of molnupiravir, Int. J. Mol. Sci. 23 (2022) 1508.
[27] L.E. Alkhimova, A.V. Sharov, T.M. Burkhanova, M.G. Babashkina, D.A. Safin, Ambroxol: insight into the crystal structure, hirshfeld surface analysis and computational study, Polycycl. Aromat. Comp. (2022), https://doi.org/10.1080/10406638.2022.2049323.
[28] M.G. Babashkina, D.A. Safin, 6-Amino-2-(4-fluorophenyl)-4-(trifluoromethyl) quinoline: insight into the crystal structure, hirshfeld surface analysis and computational study, Polycycl. Aromat. Comp. (2022), https://doi.org/10.1080/10406638.2022.2068622.
[29] M.G. Babashkina, E.V. Panova, L.E. Alkhimova, D.A. Safin, Salen: insight into the crystal structure, Hirshfeld surface analysis, optical properties, DFT and molecular docking studies, Polycycl. Aromat. Comp. (2022), https://doi.org/10.1080/10406638.2022.2097281.
[30] K.M. Kim, T. Qin, Y.-Y. Jiang, L.-L. Chen, M. Xiong, D. Caetano-Anollés, H.-Y. Zhang, G. Caetano-Anollés, Protein domain structure uncovers the origin of aerobic metabolism and the rise of planetary oxygen, Structure 20 (2012) 67–76.
[31] R.E. Olson, Karl August Folkers (1906–1997), J. Nutr. 131 (2001) 2227–2230.
[32] E. Hadjoudis, M. Vitterakis, I. Moustakali, I. Mavridis, Photochromism and thermochromism of schiff bases in the solid state and in rigid glasses, Tetrahedron 43 (1987) 1345–1360.
[33] E. Hadjoudis, I.M. Mavridis, Photochromism and thermochromism of Schiff bases in the solid state: structural aspects, Chem. Soc. Rev. 33 (2004) 579–588.
[34] K. Amimoto, T. Kawato, Photochromism of organic compounds in the crystal state, J. Photochem. Photobiol., C 6 (2005) 207–226.
[35] T. Haneda, M. Kawano, T. Kojima, M. Fujita, Thermo-to-photo-switching of the chromic behavior of salicylideneanilines by inclusion in a porous coordination network, Angew. Chem. Int. Ed. 46 (2007) 6643–6645.
[36] A. Filarowski, A. Koll, L. Sobczyk, Intramolecular hydrogen bonding in o-hydroxy aryl schiff bases, Curr. Org. Chem. 13 (2009) 172–193.
[37] V. Bertolasi, P. Gilli, G. Gilli, Crystal chemistry and prototropic tautomerism in 2-(1-Iminoalkyl)-phenols (or naphthols) and 2-Diazenyl-phenols (or naphthols), Curr. Org. Chem. 13 (2009) 250–268.
[38] E. Hadjoudis, S.D. Chatziefthimiou, I.M. Mavridis, Anils: photochromism by H-transfer, Curr. Org. Chem. 13 (2009) 269–286.
[39] V.I. Minkin, A.V. Tsukanov, A.D. Dubonosov, V.A. Bren, Tautomeric Schiff bases: iono-, solvato-, thermo- and photochromism, J. Mol. Struct. 998 (2011) 179–191.
[40] C.R. Groom, I.J. Bruno, M.P. Lightfoot, S.C. Ward, The Cambridge structural database, Acta Crystallogr. B72 (2016) 171–179.
[41] T. Fujiwara, Y. Izumi, K. Tomita, Acta Crystallogr. A28 (1972) S49.
[42] R. Dennington, T.A. Keith, J.M. Millam, GaussView, Version 6.0, Semichem Inc., Shawnee Mission: Shawnee, Kansas, 2016.
[43] M.J. Frisch, G.W. Trucks, H.B. Schlegel, G.E. Scuseria, M.A. Robb, J.R. Cheeseman, G. Scalmani, V. Barone, B. Mennucci, G.A. Petersson, H. Nakatsuji, M. Caricato, X. Li, H.P. Hratchian, A.F. Izmaylov, J. Bloino, G. Zheng, J.L. Sonnenberg, M. Hada, M. Ehara, K. Toyota, R. Fukuda, J. Hasegawa, M. Ishida, T. Nakajima, Y. Honda, O. Kitao, H. Nakai, T. Vreven, J.A. Montgomery Jr., J.E. Peralta, F. Ogliaro, M. Bearpark, J.J. Heyd, E. Brothers, K.N. Kudin, V.N. Staroverov, T. Keith, R. Kobayashi, J. Normand, K. Raghavachari, A. Rendell, J.C. Burant, S.S. Iyengar, J. Tomasi, M. Cossi, N. Rega, J.M. Millam, M. Klene, J.E. Knox, J.B. Cross, V. Bakken, C. Adamo, J. Jaramillo, R. Gomperts, R.E. Stratmann, O. Yazyev, A. J. Austin, R. Cammi, C. Pomelli, J.W. Ochterski, R.L. Martin, K. Morokuma, V. G. Zakrzewski, G.A. Voth, P. Salvador, J.J. Dannenberg, S. Dapprich, A.D. Daniels, O. Farkas, J.B. Foresman, J.V. Ortiz, J. Cioslowski, D.J. Fox, Gaussian 09, Revision D.01, 2013.

[44] R. Krishnan, J.S. Binkley, R. Seeger, J.A. Pople, Self-consistent molecular orbital methods. XX. A basis set for correlated wave functions, J. Chem. Phys. 72 (1980) 650–654.
[45] A.D. Becke, Density-functional thermochemistry. III. The role of exact exchange, J. Chem. Phys. 98 (1993) 5648–5652.
[46] M.J. Frisch, J.A. Pople, J.S. Binkley, Self-consistent molecular orbital methods 25. Supplementary functions for Gaussian basis sets, J. Chem. Phys. 80 (1984) 3265–3269.
[47] N.M. O'boyle, A.L. Tenderholt, K.M. Langner, cclib: a library for package-independent computational chemistry algorithms, J. Comput. Chem. 29 (2008) 839–845.
[48] http://gausssum.sourceforge.net/.
[49] O. Trott, A.J. Olson, AutoDock Vina: improving the speed and accuracy of docking with a new scoring function, efficient optimization, and multithreading, J. Comput. Chem. 31 (2010) 455–461.
[50] J. Eberhardt, D. Santos-Martins, A.F. Tillack, S. Forli, AutoDock Vina 1.2.0: new docking methods, expanded force field, and Python bindings, J. Chem. Inf. Model. 61 (2021) 3891–3898.
[51] Y. Rose, J.M. Duarte, R. Lowe, J. Segura, C. Bi, C. Bhikadiya, L. Chen, A.S. Rose, S. Bittrich, S.K. Burley, J.D. Westbrook, RCSB protein data bank: architectural advances towards integrated searching and efficient access to macromolecular structure data from the PDB archive, J. Mol. Biol. 433 (2021), 166704.
[52] BIOVIA, Dassault Systèmes, BIOVIA Discovery Studio, Dassault Systèmes, San Diego, 2020, 2020.
[53] A. Daina, O. Michielin, V. Zoete, SwissADME: a free web tool to evaluate pharmacokinetics, drug-likeness and medicinal chemistry friendliness of small molecules, Sci. Rep. 7 (2017), 42717.
[54] http://www.swissadme.ch/.
[55] A. Diana, V. Zoete, A BOILED-egg to predict gastrointestinal absorption and brain penetration of small molecules, ChemMedChem 11 (2016) 1117–1121.
[56] P. Banerjee, A.O. Eckert, A.K. Schrey, R. Preissner, ProTox-II: a webserver for the prediction of toxicity of chemicals, Nucleic Acids Res. 46 (2018) w257–w263.
[57] https://tox-new.charite.de/protox_II/index.php?site=home.
[58] http://www.gromacs.org.
[59] L. Sobczyk, S.J. Grabowski, T.M. Krygowski, Interrelation between H-bond and pi-electron delocalization, Chem. Rev. 105 (2005) 3513–3560.
[60] C.P. Frizzo, M.A.P. Martins, Aromaticity in heterocycles: new HOMA index parametrization, Struct. Chem. 23 (2012) 375–380.
[61] I.B. Obot, D.D. Macdonald, Z.M. Gasem, Density functional theory (DFT) as a powerful tool for designing new organic corrosion inhibitors. Part 1: an overview, Corrosion Sci. 99 (2015) 1–30.
[62] M. Goyal, S. Kumar, I. Bahadur, C. Verma, E.E. Ebenso, Organic corrosion inhibitors for industrial cleaning of ferrous and nonferrous metals in acidic solutions: a review, J. Mol. Liq. 256 (2018) 565–573.
[63] T.J. Harvey, F.C. Walsh, A.H. Nahlé, A review of inhibitors for the corrosion of transition metals in aqueous acids, J. Mol. Liq. 266 (2018) 160–175.
[64] D.S. Chauhan, C. Verma, M.A. Quraishi, Molecular structural aspects of organic corrosion inhibitors: experimental and computational insights, J. Mol. Struct. 1227 (2021), 129374.
[65] A. Kokalj, Molecular modeling of organic corrosion inhibitors: calculations, pitfalls, and conceptualization of molecule-surface bonding, Corrosion Sci. 193 (2021), 109650.
[66] I. Gotman, Characteristics of metals used in implants, J. Endourol. 11 (1997) 383–389.
[67] G. Manivasagam, D. Dhinasekaran, A. Rajamanickam, Biomedical implants: corrosion and its prevention - a review, Recent Pat. Corros. Sci. 2 (2010) 40–54.
[68] D. Aggarwal, V. Kumar, S. Sharma, Drug-loaded biomaterials for orthopedic applications: a review, J. Contr. Release 344 (2022) 113–133.
[69] H.B. Michaelson, The work function of the elements and its periodicity, J. Appl. Phys. 48 (1977) 4729–4733.
[70] P. Geerlings, F. De Proft, W. Langenaeker, Conceptual density functional theory, Chem. Rev. 103 (2003) 1793–1874.
[71] P. Pérez, L.R. Domingo, A. Aizman, R. Contreras, Chapter 9 the electrophilicity index in organic chemistry, in: A. Toro-Labbé (Ed.), Theoretical and Computational Chemistry, 19, Elsevier B.V., 2007, pp. 139–291.
[72] A. Eme, S.M. Sağdınç, Spectroscopic (FT–IR, FT–Raman, UV–Vis) analysis, conformational, HOMO-LUMO, NBO and NLO calculations on monomeric and dimeric structures of 4–pyridazinecarboxylic acid by HF and DFT methods, J. Mol. Struct. 1147 (2017) 322–334.
[73] X.-Y. Meng, H.-X. Zhang, M. Mezei, M. Cui, Molecular docking: a powerful approach for structure-based drug discovery, Curr. Comp. Aid. Drug 7 (2011) 146–157.
[74] W.L. Jorgensen, The many roles of computation in drug discovery, Science 303 (2004) 1813–1818.
[75] H. Li, H.-Y. Wang, S. Kang, R.B. Silverman, T.L. Poulos, Electrostatic control of isoform selective inhibitor binding in nitric oxide synthase, Biochemistry 55 (2016) 3702–3707.
[76] https://www.who.int/emergencies/disease-outbreak-news/item/2022-DON385.